The Astrophysical Journal, 595:483–492, 2003 September 20

TRACE AND *YOHKOH* OBSERVATIONS OF A WHITE-LIGHT FLARE

Thomas R. Metcalf,[1] David Alexander,[1] Hugh S. Hudson,[2]
and Dana W. Longcope[3]
Received 2003 January 27; accepted 2003 May 31

ABSTRACT

We present observations of a large solar white-light flare observed on 2001 August 25, using data from the *Transition Region and Coronal Explorer* (*TRACE*) white-light channel and *Yohkoh*/HXT. These emissions are consistent with the classic type I white-light flare mechanism, and we find that the enhanced white-light emission observed by *TRACE* originates in the chromosphere and temperature minimum regions via nonequilibrium hydrogen ionization induced by direct collisions with the electron beam and by back-warming of the lower atmosphere. The three flare kernels observed in hard X-rays and white light are spatially associated with magnetic separatrices, and one of the kernels is observed to move along a magnetic separatrix at 400 km s^{-1}. This is evidence in favor of particle acceleration models, which energize the electrons via magnetic reconnection at magnetic separators.

Subject headings: Sun: chromosphere — Sun: flares — Sun: X-rays, gamma rays

1. INTRODUCTION

White-light flares (WLFs), first observed by Carrington (1859), are typically the most energetic of solar flares. "White light" (WL) refers to continuum emission in excess of the photospheric background, and for extreme cases (such as Carrington's) the local intensity may actually double. The energy implied by this rivals that observed in any of the flare effects observed in the much more tenuous corona. In recent decades it has become clear that the WLF continuum formation has a strong association with particle acceleration, specifically quasi-relativistic electrons (Rust & Hegwer 1975; Hudson et al. 1992; Neidig & Kane 1993). Thus, the most ancient of solar flare measurements pointed already to the key elements of flare physics recognized only in recent decades. In this respect, it is also interesting to note that the first observed flare was also the first "geoeffective" flare (see Chapman & Bartels 1940 for a reproduction of the data for the original geomagnetic effects).

In the meantime, research on the actual optical spectrum of WLFs, and an understanding of its physics, proceeded rather slowly because of the great difficulty of the observation. The WL continuum is a phenomenon of the impulsive phase and occurs near sunspots, where seeing conditions strongly affect photometry at low contrast. Accordingly, high time resolution and seeing-free observations have paramount importance, and the absence of these conditions led to the probably erroneous belief that the WLF phenomenon only occurred in rare, unusual flares. But in *Yohkoh* observations—the first from space—WLF emission occurred down to the fundamental limit of photon counting statistics, in proportion with other measures of flares, such as the *GOES* class (Hudson et al. 1992; Sylwester & Sylwester 2000; Matthews et al. 2002).

WLFs fall into two general categories, type I and type II (Machado et al. 1986). The more common type I events show strong and broadened hydrogen Balmer lines and a Balmer and Paschen jump and demonstrate a good correlation between the continuum emission and the hard X-ray (HXR) and microwave bursts (Fang & Ding 1995), indicating that the type I WLF is closely connected with flare energy deposition by nonthermal particles in the chromosphere. The continuum emission is produced predominately by hydrogen recombination, and energy transport to lower levels in the atmosphere is by radiative back-warming (Hudson 1972; Metcalf et al. 1990a; Metcalf, Canfield, & Saba 1990b; Ding & Fang 1996). The type II events do not show this strong chromospheric effect, and Ding, Fang, & Yun (1999) suggest that type II WLFs are the result of energy release in the photosphere or temperature minimum region, although this has yet to be verified observationally.

Our main purposes in this paper are to examine the utility of the *Transition Region and Coronal Explorer* (*TRACE*) WL channel (Handy et al. 1999) for studying WLFs and to understand where and how the continuum emission observed in the *TRACE* WL channel is formed. We accomplish this in the context of a remarkable X5.3 solar flare observed on 2001 August 25 (see also Kaufmann et al. 2002 for a discussion of the high-energy phenomena in this event). This paper introduces a new set of WLF data obtained with the very high spatial resolution afforded by *TRACE*. The flare occurred near disk center (S17°, E34°) and therefore provides us with an excellent opportunity to study the magnetic mapping of the coronal field into the footpoint regions precisely determined with *TRACE* WL and with the *Yohkoh* Hard X-ray Telescope (HXT; Kosugi et al. 1991).

The relationship between the coronal structure of a solar flare and its structure as observed in the lower solar atmosphere (including the magnetograms) remains unclear. The HXR footpoints map to the site of particle acceleration and also, therefore, to a main source of energy release (see, e.g., Fletcher & Hudson 2001). In this event, we find remarkable coincidences between the magnetic separatrices (which indicate the coronal magnetic topology) and the features,

[1] Lockheed Martin Solar and Astrophysics Laboratory, Department L9-41, Building 252, 3251 Hanover Street, Palo Alto, CA 94304.
[2] Space Science Laboratory, University of California, Berkeley, CA 94720.
[3] Department of Physics, Montana State University, Bozeman, MT 59717.

including flare ribbons, delineated by the WL and HXR observations. We discuss the interpretation of these observations in terms of current models.

2. OBSERVATIONS

On 2001 August 25, an impulsive X5.3 flare was observed by a number of observatories. The flare occurred in NOAA Active Region 9591 at S17°, E34°, and the initial rise in HXRs was observed at about 16:29 UT. Here we are concerned primarily with observations made by the *TRACE*, *Yohkoh*, and *SOHO*/MDI spacecraft. The flare was well observed by both *Yohkoh* and *TRACE*, with MDI magnetic field data available 1.5 hr after the event. Unfortunately, no MDI WL data were available during the flare.

The *TRACE* data in the WL channel have a variable cadence, with WL images typically every 1.5–2.5 minutes. The *TRACE* WL channel has a very broad response, from 1700 Å to 1 μm. Figure 1 shows the response to the solar spectrum suggested by Handy (1998). Since the response is so broad, the *TRACE* WL channel is sensitive to emission in the transition region, chromosphere, and photosphere. While the lack of spectroscopic resolution is a disadvantage of the *TRACE* data, the high spatial resolution and the broad spectral response make the data set very useful for examining the morphology of the WL emission. In particular, the broad spectral response means that *TRACE* observes essentially all the continuum emission in the flare and provides an excellent tool for understanding the energetics of the WL emission.

Figure 2 shows a sequence of *TRACE* images in the WL channel with the closest-in-time *Yohkoh*/HXT HXR contours overlaid. The HXT images were calculated using the pixon algorithm described by Metcalf et al. (1996). There is an excellent correspondence between the HXR sources and the brightest WL sources. However, the correspondence does not hold at all locations of WL emission. This is most likely a consequence of the limited dynamic range in the HXT images (10 : 1); weak HXR emission over the weaker WL sources cannot be imaged in the presence of the much brighter HXR sources over the northern part of the flare (see, e.g., Alexander & Metcalf 1997).

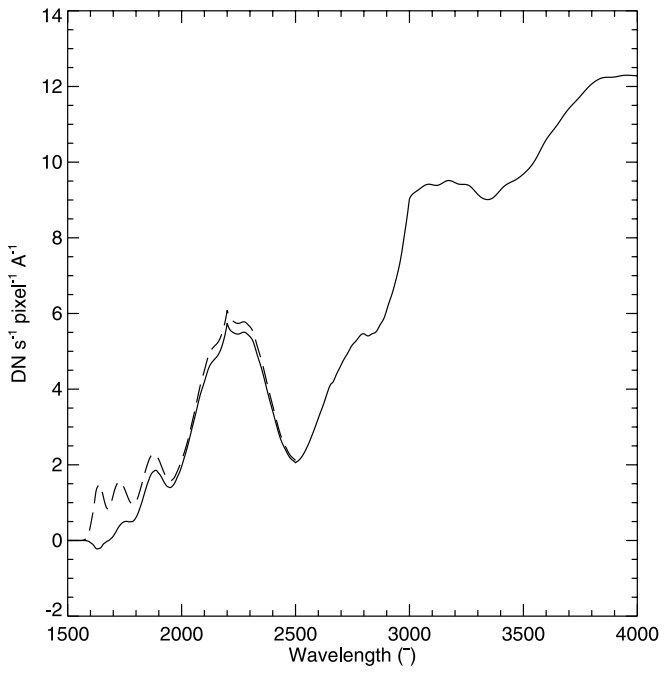

FIG. 1.—Response of the *TRACE* WL channel in the UV and the blue (*dashed line*). The *TRACE* WL channel is sensitive to light well to the red of that shown in the figure. The solid line shows the response after subtracting the *TRACE* 1700 Å UV channel.

Figure 3 shows *TRACE* difference images, to highlight the WLF emission by removing the static sunspot features. Figures 2 and 3 show all the available *TRACE* WL data during the flare impulsive phase. During this time interval, there were many more HXR images than *TRACE* images, and we have overlaid the *TRACE* data with the nearest HXR image.

The flare had three main parts visible in the WL images and the HXR contours at 16:31:23. In the northern portion of the event, there are two WL ribbons running north-south, and in the southern portion of the event, there is a third ribbon running east-west, although this may be an extension of the eastern ribbon to the north. The HXR emission is primarily located over the two northern ribbons, but there is also significant HXR emission over the southern ribbon. The reconstructed HXR sources are larger in spatial extent at the peak of the impulsive phase than at the end of the impulsive phase, but it is not clear whether this is a real effect or an artifact of the HXR image reconstruction. At any rate, the HXRs are clearly associated with the sunspot umbrae and move across the sunspots as the flare progresses.

The HXRs were clearly nonthermal in nature, and a thick-target fit to the HXT M1 and M2 channels gives an electron spectral index of 3 at the peak of the HXR flare (16:31–16:32 UT). This spectral index was consistent over all three of the main flare ribbons. The HXR spectrum showed a typical soft-hard-soft evolution in the spectral index, with the thick-target electron spectral index reaching as high as 6 at the start of the flare and again near the end of the impulsive phase.

Figure 4 shows the *SOHO*/MDI vertical magnetic field overlaid on the *TRACE* WL image at the peak of the flare. The vertical field was computed using a potential field calculation, with the MDI line-of-sight magnetic field as the boundary condition. The *TRACE* image is a negative image in this figure to better highlight the relationship between the WLF kernels and the magnetic field: the bright kernels are dark, and the dark sunspots are bright.

To co-align the MDI, *TRACE*, and HXT data, we used the known pointing of the MDI WL image, obtained at the time of the magnetic field measurement, to correct the not-so-well-known *TRACE* pointing with a cross correlation between the *TRACE* and MDI WL data. The *TRACE* pointing correction also accounts for the parallax between the Earth view and the L1 view, solar rotation, and foreshortening. The adjustment to the raw *TRACE* pointing was about 7″, and we estimate the accuracy of the alignment between the *TRACE* WL data and the MDI magnetogram to be about a *TRACE* pixel (0.″5). The HXT data are aligned using the known *Yohkoh* pointing, and we estimate the accuracy to be 2.″5 or better.

Figure 5 shows the *TRACE* 284 Å channel overlaid with the HXT contours. The data from the 284 Å channel have a larger field of view than the WL data, so this data set gives a more global view of the flare. Late in the flare (*bottom right-hand panel*), it is easy to see that there is flare-related

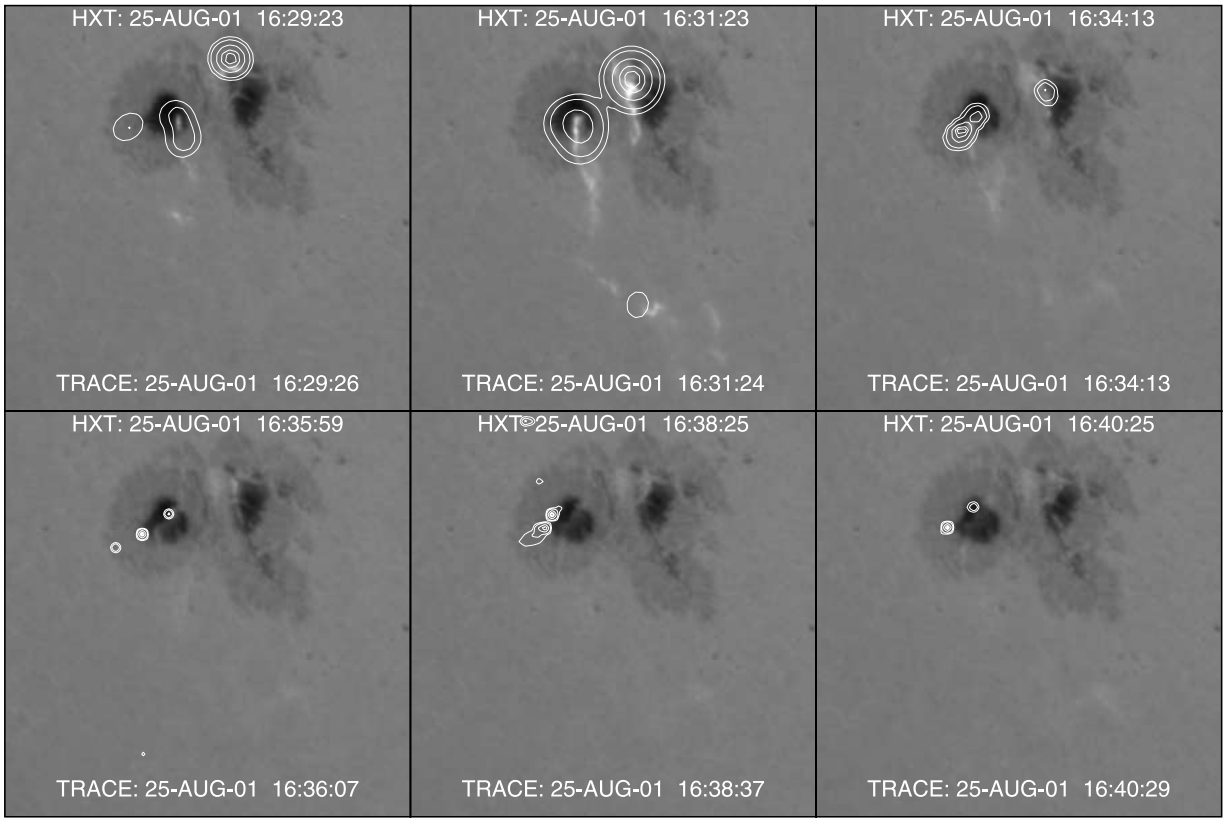

FIG. 2.—Development of the WLF as a function of time. The *TRACE* WL data are displayed as an image and the HXT HXRs (M2 channel, 33–53 keV) as contours. The images are 300 *TRACE* pixels, or 150″, on a side. The contours may not accurately represent the HXR source sizes.

emission considerably farther to the south than we can see in the WL data. Whether this part of the flare also emits continuum radiation is not known. At any rate, there is a good spatial correspondence between the 284 Å, WL, and HXR data. This is to be expected if the nonthermal electron beam responsible for the HXR emission gives the primary energization of the flare and is ultimately responsible for both the chromospheric/photospheric continuum emission and the emission seen in the 284 Å channel. The ribbon structure visible in the 284 Å images shows that the 284 Å emission is concentrated at the footpoints of the flare arcade, rather than in filled loops.

Both the eastern and western flare ribbons in the northern section of the flare are associated with sunspot umbrae, with the eastern kernel of WL and HXR emission moving across the umbra as the flare progresses. The motion of the three main footpoint sources is indicated in Figure 6. The eastern footpoint initially moves to the northeast, into the sunspot umbra, before spreading out across the umbra at late times in the impulsive phase (red in Fig. 6), with the main source moving to the southeast. The western footpoint initially moves to the southeast, before turning to the southwest at about 16:31:30. The southern footpoint moves rapidly to the southwest early in the impulsive phase, although there is also a stationary component until about 16:34. This stationary component disappears after this, but this may simply be due to the brightening of the eastern and western footpoints and the lack of dynamic range in HXT.

Figure 7 complements Figure 6, showing the source brightness rather than the time. The combination of these figures details the evolution of the HXR flare. The plus signs show the location of the centroid of the HXR emission for each of the three main HXR sources. The spatial extent is not coded into the figures, but can be discerned from Figures 2, 3, and 5, with the caveat that the source size is not always reliably reconstructed.

The most southerly HXR source (Fig. 2; 16:31:23) is particularly interesting. This source of HXRs moved along the southern ribbon of WL emission at a speed of about 400 km s^{-1} (Fig. 8). After 16:31:10, the southern HXR emission disappears, although it is likely that it is simply lost when the main footpoints become very bright, since the dynamic range of HXT is insufficient to reveal the weaker southern source in the presence of the bright northern sources.

To understand how the flare morphology revealed by the HXR and WL emission relates to the magnetic field observed in the MDI data, we have computed the magnetic topology of the active region using a potential field extrapolation of the MDI data. This simple model is sufficient to understand the global connectivity of the magnetic field in the active region, but we do not attempt to interpret the details of the potential field model in the corona. We compute field lines from every MDI pixel and find the location of the opposite footpoint along the field line. We then look for discontinuities in the location of the far footpoint between adjacent pixels. These discontinuities, shown in Figure 9, delineate the intersections of magnetic separatrices with the lower boundary. Remarkably, the southern HXR source, which is observed to move southwestward at 400 km s^{-1}, is in fact moving along a magnetic separatrix, while the

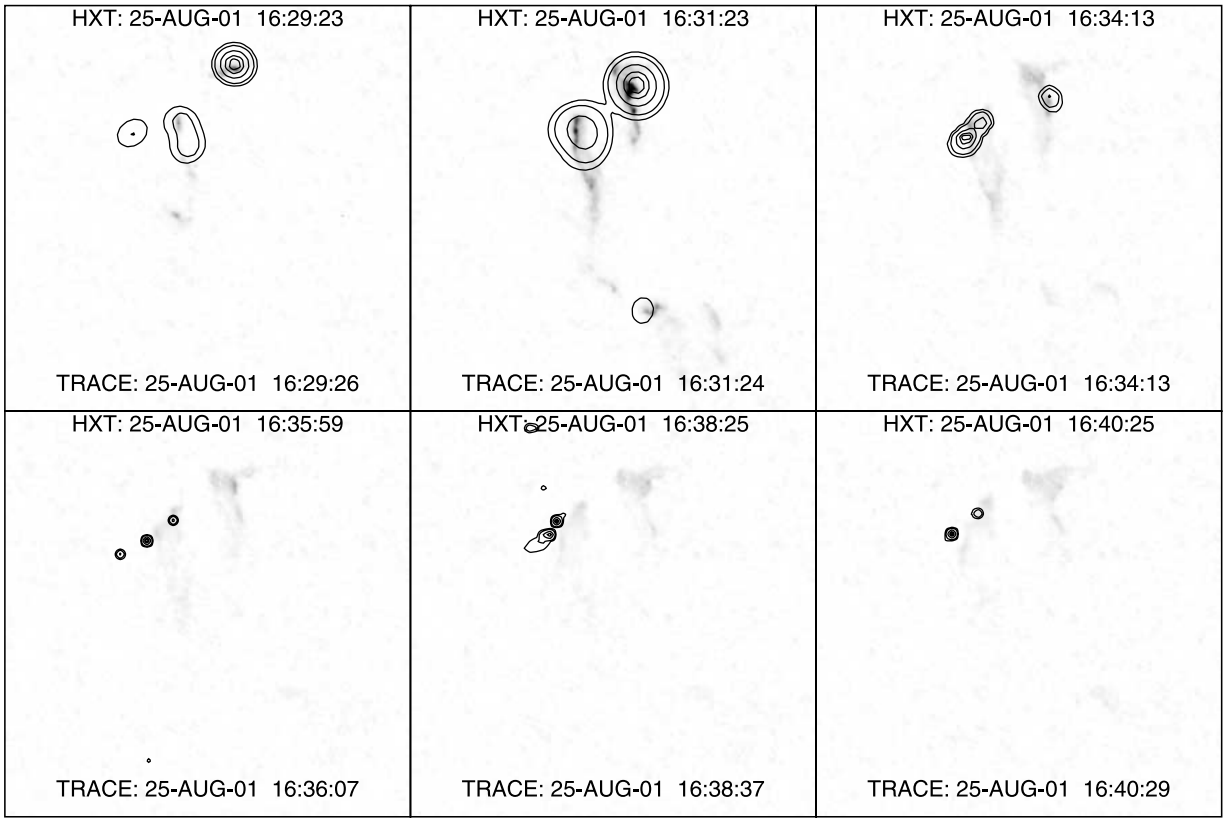

FIG. 3.—*TRACE* WL difference images for the event with the HXR contours (M2 channel, 33–53 keV). The difference images are for the *TRACE* image at 16:20:01 UT minus the *TRACE* image at the displayed time. Hence, the bright WL emission is dark in the images. The contrast has been enhanced to bring out the fainter features.

northern footpoints are evolving toward the northern separatrices, calculated at a time 1.5 hr after the flare. We discuss the implications of this observation below.

3. ANALYSIS

The *TRACE* WL channel has a very broad response, so the question naturally arises at what wavelengths the WL emission is enhanced. One possibility is that the enhanced WL emission is in fact UV. However, this can be readily checked by using the *TRACE* 1700 Å channel. The 1700 Å channel on *TRACE* uses the 1600 Å analysis filter in series with the fused silica WL filter. Hence, the 1700 Å channel is well suited to detecting any UV continuum that may be present in the *TRACE* WL images.

The solid line in Figure 1 shows the spectral response after subtracting the *TRACE* 1700 Å channel from the WL channel. The 1700 Å data must be normalized to the WL exposure time and scaled to account for the transmission of the 1600 Å channel filter before subtraction. This procedure uses the 1600 Å response weighted by the solar UV intensity at each wavelength and hence depends somewhat on the solar spectrum in the 1600–2000 Å range. We used the spectrum suggested by Handy (1998) for this purpose and multiply the exposure-normalized 1700 Å image by 7 before subtracting. Although this is not a flare spectrum, the result is not highly dependent on the spectrum chosen, as it is the magnitude of the weighted 1600 Å response that we require. A different spectrum would weight the response differently, but the response is sufficiently flat so that the factor of 7 could not reasonably change by more than a factor of 2. Figure 10 demonstrates that there is very little UV in the *TRACE* WL channel for this flare, regardless of the precise value of the 1700 Å multiplicative factor.

Figures 11, 12, and 13 show the light curves for each of the three flare kernels in HXR, 1700 Å, and WL-1700. In each of the three flare kernels observed on August 25, the *TRACE* 1700 Å emission brightens for a considerably longer time than the HXRs and the WL. This further indicates that the WL-1700 Å emission is not significantly contaminated by UV continuum. Also, despite the poor temporal resolution of the *TRACE* WL data, it is clear that the WL emission in the northwest and northeast kernels closely follows the HXR emission. This correspondence is less clear in the south kernel, as there is low-level WL emission late in the flare. At the peak of the event, the brightest *TRACE* WL pixels are saturated (10 pixels), so that we have slightly underestimated the total intensity of WL emission.

The close correspondence between the HXR and WL emission strongly suggests that this flare was a type I WLF. Hence, we expect that the continuum emission was energized by the nonthermal electron beam, which also produced the HXR emission. Although the *TRACE* WL data have no spectral resolution, we can expect strong and broadened Balmer lines, as well as a Balmer and Paschen jump, based on the assumption that the flare is a type I. The WL emission in this case is generated throughout the chromosphere and temperature minimum region as ionized hydrogen recombines (Hudson 1972). It is not necessary for the electron beam to penetrate to the lower chromosphere,

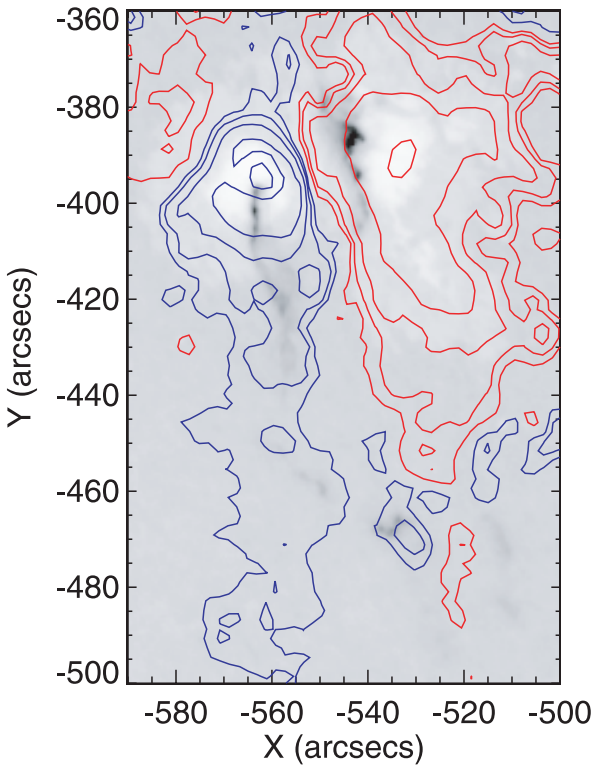

FIG. 4.—Negative image of the *TRACE* WL data at 16:31:23 overlaid with contours of the vertical magnetic field derived from the nearest MDI observation, at 17:57:30 UT. The red contours show upward field, and the blue contours show downward field. The contour levels are set at 100, 200, 400, 800, and 1600 G. Solar north is up, and solar east is to the left. The axes are labeled in arcseconds from the disk center.

since the energy is transported to the lower atmosphere via back-warming (Metcalf et al. 1990a, 1990b). The Metcalf et al. (1990a, 1990b) observations demonstrate that, although the atmospheric density decreases with height in the chromosphere, this is offset by the increasing ionization fraction in the presence of back-warming, so that the flare-enhanced electron density is constant throughout the chromosphere, with a typical value of $n_e = 3 \times 10^{12}$ cm^{-3}.

Since the flare is a type I event, we postulate that the enhanced WL emission seen in the *TRACE* images is coming from the chromosphere and temperature minimum region and is primarily Balmer and Paschen continuum emission resulting from the nonequilibrium ionization caused by electron beam collisions and back-warming (Hudson 1972; Metcalf et al. 1990b). We verify this proposed mechanism from a number of expected effects. First, we have already noted the close spatial correspondence between the HXR and enhanced WL. Second, if the *TRACE* WL emission in the flare kernels is coming from the chromosphere, we expect that it will track the HXR emission temporally, since the recombination time for hydrogen is $\lesssim 1$ s in the chromosphere and temperature minimum region, considerably shorter than the cadence of *TRACE* images for this event. The UV emission comes from higher in the atmosphere, where the excitation is dependent not on the electron beam but on the conduction of energy from the corona, resulting in a more gradual development of the *TRACE* 1700 Å UV channel. Although it is possible for the UV and EUV emission in a flare to cause photoionization in the chromosphere (Emslie & Machado 1979; Machado & Hénoux 1982), the *TRACE* light curves show that this is not a dominant mechanism, at least in this flare. Since these photoionizations primarily affect neutral carbon and silicon (Machado & Hénoux 1982), the electron density enhancement cannot be sufficient to explain the observed WL enhancement.

Third, we verify the chromospheric origin of the *TRACE* WL emission by examining the energetics of the HXR and WL emissions. Using a thick-target model for the HXR production (see, e.g., Brown 1971 or Tandberg-Hanssen & Emslie 1988), we compute the power carried by the nonthermal electrons as

$$P_e(E_0) = \frac{4\pi R^2 C}{\kappa_{\rm BH}\bar{Z}^2}\frac{\delta - 1}{B(\delta - 2, 1/2)} a E_0^{2-\delta} , \qquad (1)$$

where $R = 1$ AU, $C = 2\pi e^4 \ln\Lambda$, $\kappa_{\rm BH}$ is the constant in the Bethe-Heitler bremsstrahlung cross section, B is the beta function, $aE^{-\gamma}$ is the HXR photon spectrum, $\delta = \gamma + 1$ is the electron spectral index, and E_0 is the lower energy cutoff in the electron spectrum. With the electron thick-target spectral index of $\delta = 3$ computed from the HXT M1 and M2 channels, the HXT M2 data at the peak of the flare imply a total flare power in the form of accelerated electrons of 3×10^{29} ergs s^{-1} above 20 keV or 6×10^{29} ergs s^{-1} above 10 keV, depending on the (unknown) lower energy cutoff for the accelerated electrons.

We compare this power in nonthermal electrons to the power radiated in the wavelengths observed by the *TRACE* WL channel. To do this properly, we need to know the spectrum of the radiation observed by *TRACE*: although we know the *TRACE* response, we do not know the energy of the photons observed by *TRACE*, since the *TRACE* WL data have no spectral resolution. So, to make a simple estimate of the power in the WL, we assume that all the WL emission above the preflare emission is from the Balmer and Paschen continua and verify the consistency of this assumption against the HXR power. We neglect the ground state of hydrogen, using the "on-the-spot" approximation (see, e.g., Osterbrock 1989), while continuing to consider transitions from the continuum to the second and third hydrogen levels, plus the Hα transition from level 3 to level 2. The on-the-spot approximation is excellent in the chromosphere, where the mean free path of a Lyman continuum photon is about 20 cm. In our simple model, we neglect collisional deexcitations, so that every transition to level 2 from the continuum gives a Balmer photon and every transition from the continuum to level 3 gives a Paschen photon plus an Hα photon. This gives the enhanced power in the WL channel as

$$P_{\rm wl} = 2\pi A I\left[\frac{f_b\bar{\epsilon}_b}{T_b} + f_p\left(\frac{\bar{\epsilon}_p}{T_p} + \frac{\epsilon_\alpha}{T_\alpha}\right)\right] = 1.1 \times 10^{21} I \text{ ergs s}^{-1} , \qquad (2)$$

where I is the flare-enhanced count rate in the *TRACE* WL channel in units of DN s^{-1}, A is the area of a *TRACE* pixel (1.3×10^{15} cm^2), T_b, T_p, and T_α are the *TRACE* response at the Balmer jump, the Paschen jump, and Hα in units of DN s^{-1} photon^{-1} cm^{-2} s^{-1} sr^{-1} (5.2×10^{-17}, 4.9×10^{-17}, and 4.6×10^{-17}, respectively), f_b and f_p are the fractions of the continuum recombinations producing Balmer and Paschen photons (using the recombination rates at 5000 K, the

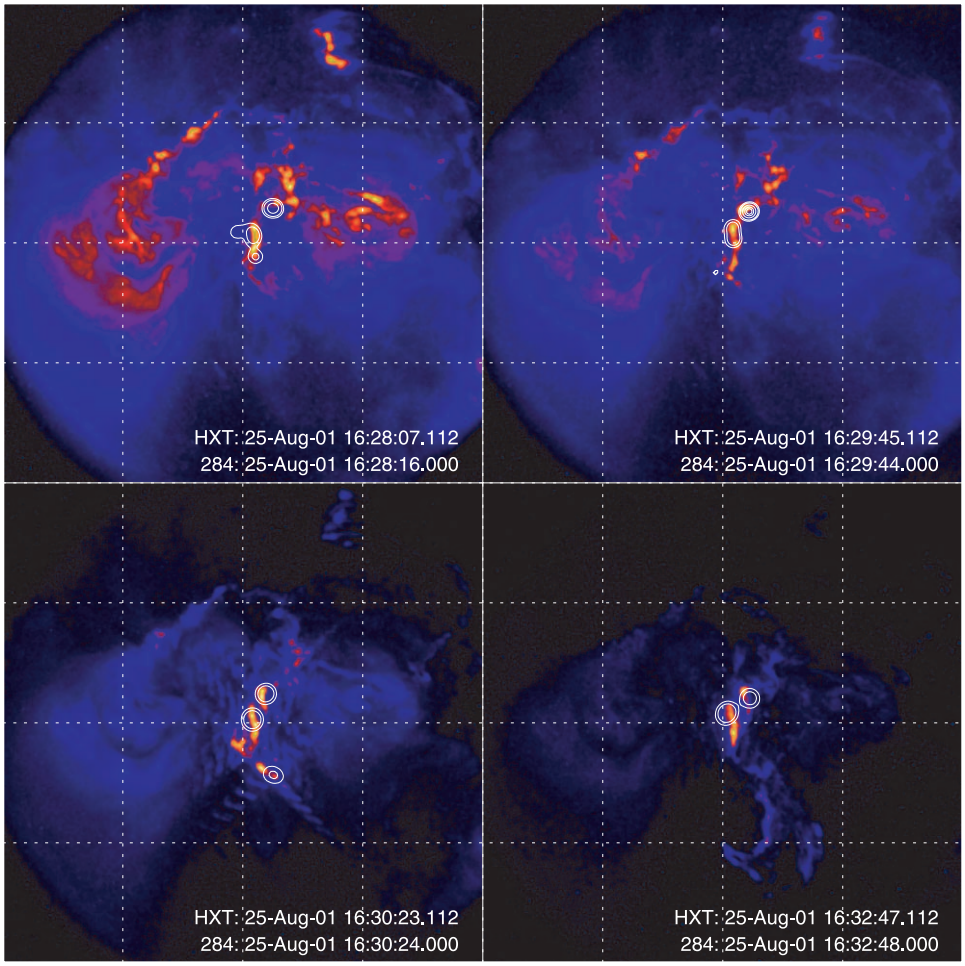

FIG. 5.—*TRACE* 284 Å channel overlaid with HXT M2 contours. Each image is independently scaled. The grid of dotted lines can be used to compare locations from one frame to the next and have a spacing of 64″.

enhancement in the WL emission will be 60% Balmer and 40% Paschen; see, e.g., Cillié 1932), and $\bar{\epsilon}_b$, $\bar{\epsilon}_p$, and ϵ_α are the photon energies for the Balmer, Paschen, and Hα transitions, respectively ($\bar{\epsilon}_b = \epsilon_b + kT = 4.4$ eV, $\bar{\epsilon}_p = \epsilon_p + kT =$ 2.4 eV, and $\epsilon_\alpha = 1.9$ eV, with ϵ_b the energy at the Balmer jump and ϵ_p the energy at the Paschen jump). Using equation (2), we compute the enhanced WL power at the peak of the flare to be 1.6×10^{29} ergs s^{-1}, comfortably below the

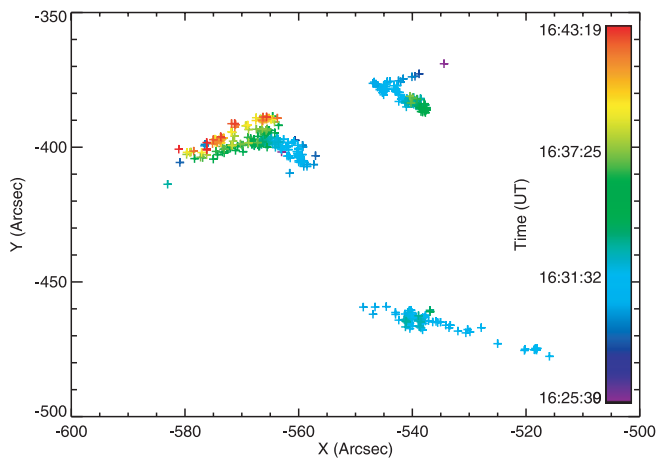

FIG. 6.—Position of the main HXR sources as a function of time. Each plus sign indicates the position of the source centroid at a single time. The color of the mark indicates the time.

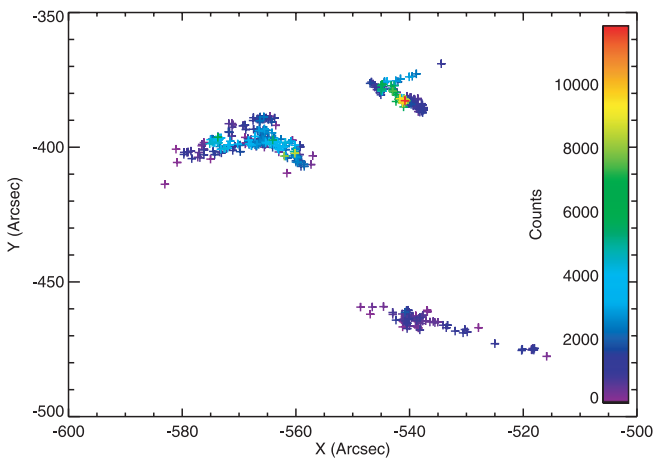

FIG. 7.—Position of the main HXR sources labeled by the footpoint brightness. Each plus sign indicates the position of the source centroid at a single time. The color of the mark indicates the source brightness.

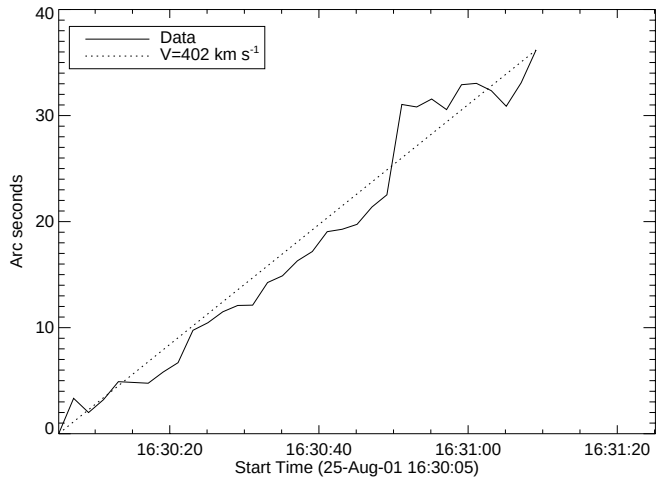

FIG. 8.—Location of the southern HXR source along the WL ribbon as a function of time. The HXR source traveled along the WL ribbon at about 400 km s^{-1}. The motion was apparently steady, with an rms uncertainty of 60 km s^{-1} over this 1 minute interval.

available power in nonthermal electrons. A more accurate treatment of the hydrogen lines and continuum would give a very similar power in the *TRACE* WL channel, since most recombinations would eventually cascade to level 2 and the *TRACE* response is reasonably flat (e.g., in eq. [2], $\bar{\epsilon}_b = \bar{\epsilon}_p + \epsilon_\alpha$, and we could neglect the Paschen term without changing the derived power if $T_b = T_p = T_\alpha$). To the extent that recombinations do not cascade all the way to level 2 (e.g., because of collisions or reionization), we have overestimated the power in the WL channel.

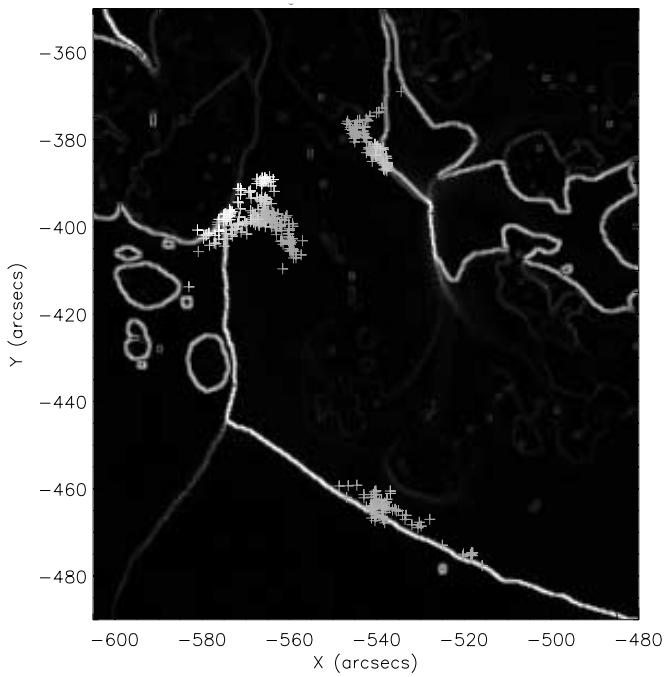

FIG. 9.—Location of the HXR sources relative to the magnetic separatrices computed from a potential field model of the active region. The plus signs show the location of the HXRs, as in Fig. 6, while the lines show the separatrices. The brightness of the separatrix indicates the magnitude of the discontinuity, with a brighter line indicating a larger discrepancy between the locations of conjugate footpoints for adjacent pixels.

We can carry the energetics argument one step further by using the neutral hydrogen ionization rate due to the nonthermal electron beam to estimate the location where the WL is formed. Hudson (1972) and Lin & Hudson (1976) introduce the fact that one ion pair is created for every $\epsilon_0 = 32$ eV of electron energy loss. With $P_e(20) = 3 \times 10^{29}$ ergs s^{-1} at the flare peak, this implies a total nonthermal ionization rate of 5.9×10^{39} s^{-1} over the entire flare. Since the recombination rate is $\alpha_B n_e^2$, the average electron density in the recombination region must be $n_e \approx 8.7 \times 10^{12}$ cm^{-3}, assuming that the preflare ionization is much less than the flare ionization:

$$\alpha_B n_e^2 \approx \frac{P_e(E_0)}{\epsilon_0 V} , \quad n_{e0} \ll n_e \ll n , \tag{3}$$

where the recombination coefficient to hydrogen levels 2 and above is given by $\alpha_B = 2.6 \times 10^{-13}$ cm^3 s^{-1} at 10^4 K and V is the volume, which we take to be the flare area of 1.5×10^{18} cm^2 times a chromospheric thickness of 2000 km ($V = 3 \times 10^{26}$ cm^3). The electron density is about 3 times the value found by Metcalf et al. (1990a), but this is not unreasonable, since the 2001 August 25 X5.3 flare was much more energetic than the M2.3 flare observed by Metcalf et al. This average density compares favorably to maximum electron densities found in WLFs by Neidig & Wiborg (1984) and Machado & Rust (1974).

We then use the ionization rate and the electron density in equation (14) of Lin & Hudson (1976) to derive the average density (n) where the recombinations are occurring:

$$\frac{dn_e}{dt} = -\alpha_B n_e^2 + \left[\beta n + \frac{P_e(E_0)}{\epsilon_0 V}\right]\left(1 - \frac{n_e}{n}\right) = 0 . \tag{4}$$

Using the value of n_e derived from equation (3),

$$n \approx \sqrt{\frac{P_e(E_0) n_e}{\epsilon_0 \beta V}} , \quad \beta \ll \frac{4 P_e(E_0)}{\epsilon_0 n_e V} , \tag{5}$$

where β represents the net radiative and collisional ionization (Lin & Hudson 1976). We compute $\beta = 4.7 \times 10^{-3}$ s^{-1} from the F1M flare model atmosphere of Metcalf et al. (1990a) and note that this is consistent with the calculation of Lin & Hudson (1976).

Equation (5) implies that the average density where the recombinations are taking place is 1.9×10^{14} cm^{-3}. Model atmospheres place this density several hundred kilometers above the temperature minimum. At this height, the preflare electron density is $n_{e0} = 10^{11}$, and with the flare electron density of 9×10^{12} cm^{-3}, the ionization is considerably enhanced over the preflare value. Hydrogen ionization is the only viable source for the increase in the electron density (Metcalf et al. 1990b). While some flare-enhanced WL emission must be spread out over the whole chromosphere, the above analysis suggests that most of it is coming from deep in the chromosphere, where the density is high and the preflare ionization is low. Note that the electron beam need not penetrate the full flare volume, since back-warming will ionize the lower atmosphere even if the electron beam is stopped in the upper chromosphere.

Figure 14 shows the thick-target HXR power above 20 keV and the WL Balmer and Paschen continuum power as a function of time. The power required to enhance the *TRACE* WL channel is less than the power available in the nonthermal electrons at all times and accounts for roughly

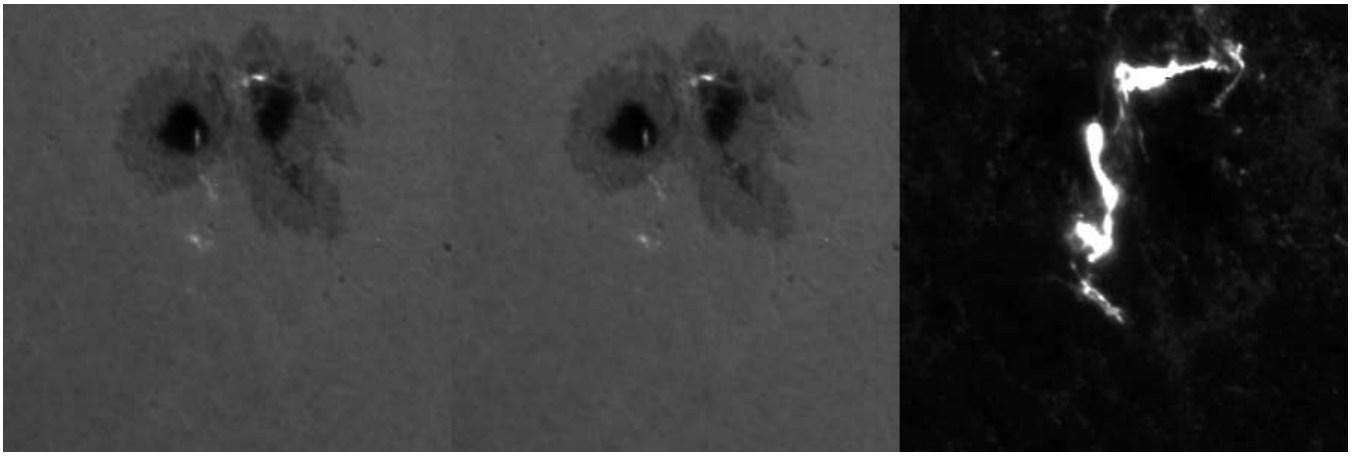

FIG. 10.—*Left*: Image from the *TRACE* WL channel at 2001 August 25 16:29:26 UT. *Middle*: *TRACE* WL data with the 1700 Å channel subtracted. There is very little difference between the left and middle images, indicating that the emission observed in the WL channel is not primarily UV. *Right*: *TRACE* 1700 Å channel image at 16:29:22 used in the subtraction.

half the available energy if the electron cutoff energy is 20 keV. This is quite reasonable, since all the flare energy deposited in the chromosphere will ultimately be radiated away, and most of this radiation will be in the *TRACE* bandpass. This fraction is consistent with the Hudson (1972) and Lin & Hudson (1976) result that one ionization occurs for every $2.5\chi_H$ of energy in the electron beam (χ_H is the hydrogen ionization energy), implying that the enhanced WL power should be $1/2.5$ of the electron power. Equivalently, the power observed in the WL channel is consistent with the flare volume and electron density derived above. This measurement is made possible by the wide bandpass of the *TRACE* WL channel: without the large bandpass, we would not be able to account for all the radiated energy observationally. Hence, our premise that the *TRACE* WL enhancement comes from the chromosphere and temperature minimum region and is primarily Balmer and Paschen continuum emission resulting from the nonequilibrium ionization caused by electron beam collisions and back-warming is fully consistent with the HXR data on the grounds of spatial colocation, timing, and energetics.

Finally, if the *TRACE* WLF emissions are coming from the chromosphere, we expect to observe *TRACE* WL enhancements in more flares than we typically see with narrowband WL emission, e.g., from *SOHO*/MDI, since the MDI bandpass is far from the Balmer or Paschen continuum enhancements (see, e.g., Donati-Falchi, Falciani, & Smaldone 1984) and WLF emission seen by MDI is very likely to be photospheric. It is much easier energetically to ionize the upper chromosphere and temperature minimum than it is to heat the photosphere, where the narrowband continuum emission is formed. This appears to be the case, as *TRACE* WLF emission is seen in a number of M-class flares above class M3 or so (e.g., the M3.6 flare on 1999 January 16 at 12:02 UT), but rarely in anything smaller than an X-class flare in the narrowband continuum (Gregory et al. 2001). This needs to be quantified and will be the subject of future research as the combined *TRACE* WL and MDI data sets are explored.

We turn now to the rapid motion of the southern HXR source along the magnetic separatrix. Magnetic separatrices

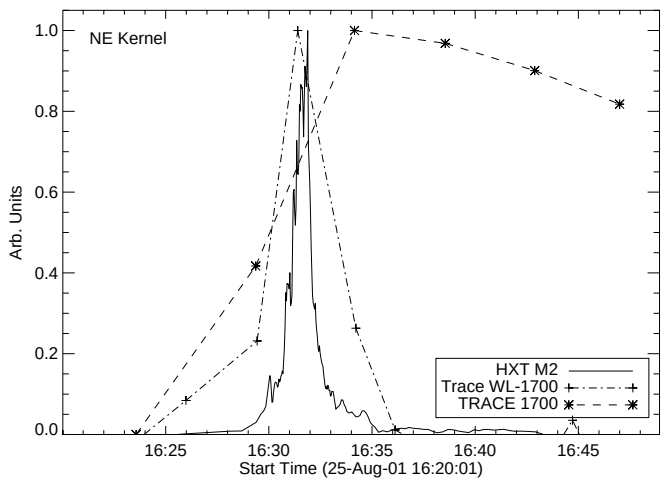

FIG. 11.—Comparison of the time development of the flare in HXRs (33–53 keV; *solid line*), *TRACE* WL (*dot-dashed line*), and UV (*dashed line*) for the northeast kernel. Each light curve is normalized to unity at its peak to facilitate intercomparison of the time development in the different wavelength bands. The WL tracks the HXR, but not the UV.

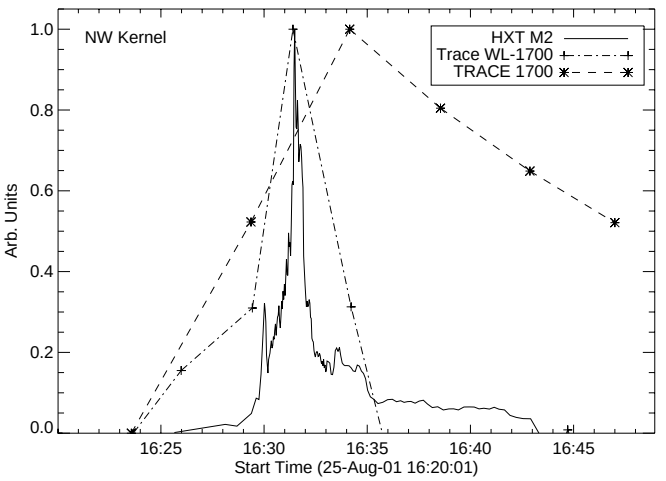

FIG. 12.—Same as Fig. 11, but for the northwest kernel

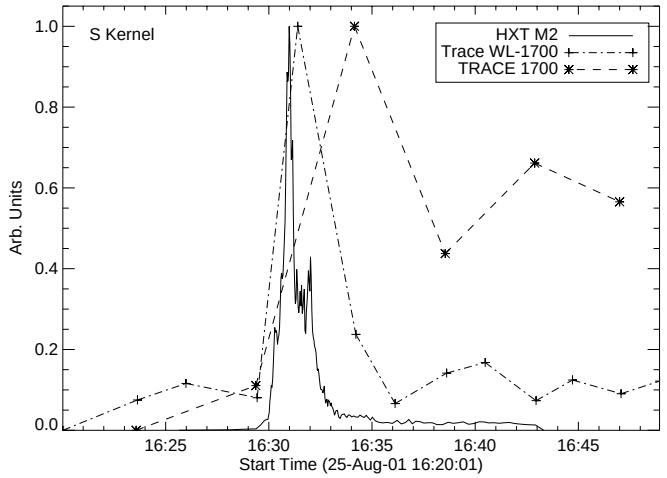

FIG. 13.—Same as Fig. 11, but for the south kernel

are surfaces across which the magnetic connectivity is discontinuous (Baum & Bratenahl 1980). The southern separatrix along which the HXR source moves lies within a region of weak negative polarity southwest of the strongest negative flux. The separatrix divides those negative pixels connecting to the nearby positive polarity just to the north from those with more distant connections.

As a magnetic field line is reconnected, its footpoints are abruptly changed, so that it must cross a magnetic separatrix (Greene 1988; Lau & Finn 1991). Since each instance of reconnection requires two field lines to exchange footpoints, the reconnection occurs along a curve called a separator, where two separatrices intersect.

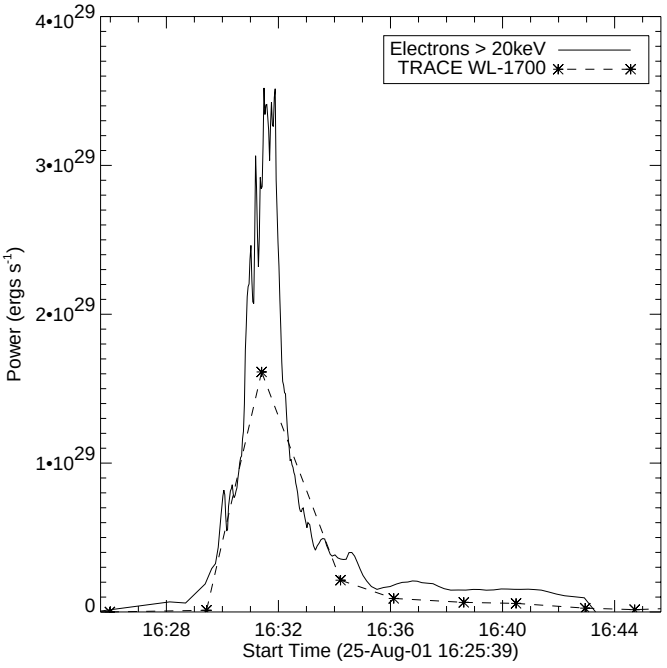

FIG. 14.—Power in nonthermal electrons, summed over all three flare kernels derived from the HXT observations using a thick-target model (*solid line*). The power input from nonthermal electrons is compared to the power radiated into the *TRACE* WL-1700 Å channel (*asterisks*).

Separatrices would be significant for flares if particle acceleration were caused by some aspect of magnetic reconnection. If this were the case, then the resulting high-energy particles would be preferentially located on those field lines that have most recently undergone reconnection. As the locus of reconnection (the separator) moves, so will the population of energetic particles. The neighborhood of the magnetic separator will include both of the separatrices whose intersection defines it. Thus, the observation of HXR footpoint emission along a separatrix is consistent with the hypothesis that reconnection leads to accelerated particles. In this case, it appears that there is a change in the amount of weak negative flux that is connected to the nearby positive flux. The westward motion along the separatrix reflects the motion of the reconnection site, which might be much slower than the apparent motion of its footpoints.

Separatrices also have a dynamical significance in addition to their topological significance. The field lines on either side of a separatrix have different footpoints, so they are likely to have different Alfvén wave oscillation periods. Field lines to the north of the separatrix connect nearby regions and will be shorter than those to the south. If there were a disturbance within the dominant bipole, its shorter field lines would react to it, while those outside the separatrix remained more still. In this scenario, there need not be reconnection of field lines, but simply discontinuous dynamical evolution. The apparent motion of the HXR footpoint would seem to reflect the speed of dynamical evolution of the interior disturbance; it would be the local Alfvén speed.

The northern HXR footpoints appear at the start of the flare to be rather distant from the separatrices. However, the footpoint motions do carry them to the separatrices by the end of the HXR event. Since the separatrices were computed with MDI data 1.5 hr after the flare impulsive phase, this is still consistent with reconnection at a separator, since the reconnection event must be dynamic to explain the motion of the southern HXR source. Hence, although the separators may not be static during the flare, they should relax to the topology revealed by the MDI data by the end of the flare. We do not have the required data to check this completely, but we can conclude that the northern footpoints are not inconsistent with the reconnection at a separator model suggested by the motion of the southern source.

4. CONCLUSIONS

We have presented observations of a large solar WLF, using data from the *TRACE* WL channel. The very high spatial resolution of *TRACE* provides some of the best WL images available, and the broad spectral response is important for understanding the energetics of the WLF. The *TRACE* 1700 Å channel is an essential complement to the WL channel, since it is possible that the WL channel would see an apparent WLF when the emission is in fact UV. The 1700 Å channel is used to eliminate this possibility.

The *TRACE* WL data set provides a new and unique view of the WLF phenomenon. In the 2001 August 25 flare, the *TRACE* WL and *Yohkoh*/HXT emissions are consistent with the classic type I WLF and originate in the chromosphere and temperature minimum region. The ultimate cause of the enhanced WL emission is the ionization and subsequent recombination of hydrogen. Energy deposited

in the chromosphere by the electron beam is transported to the lower atmosphere by back-warming.

One of the three flare kernels observed in HXR and WL moved along a magnetic separatrix at 400 km s^{-1}. This is to be expected if the nonthermal particles responsible for the HXR event are accelerated at a site of magnetic reconnection occurring at a magnetic separator. This is evidence in favor of this model of particle acceleration and is consistent with the motion of the northern footpoints, which move to the site of the postevent separatrices by the end of the flare.

Future work on WLFs utilizing *TRACE* data will focus on WL data with much higher temporal cadence, in conjunction with *Reuven Ramaty High Energy Solar Spectroscopic Imager* (*RHESSI*) HXR data. In principle, *TRACE* should be able to observe in the WL and 1700 Å channels with 2 s cadence during special campaigns. Events with simultaneous MDI WL data will be particularly useful, since the MDI continuum is photospheric and will help nail down the location where the emission observed in the *TRACE* WL channel is formed.

This work was supported by NASA contracts NAS 8-00119 and NAG 5-12878. *Yohkoh* was a mission of ISAS in Japan, with contributions from the US and UK.

REFERENCES

Alexander, D., & Metcalf, T. R. 1997, ApJ, 489, 442
Baum, P. J., & Bratenahl, A. 1980, Sol. Phys., 67, 245
Brown, J. C. 1971, Sol. Phys., 18, 489
Carrington, R. C. 1859, MNRAS, 20, 13
Chapman, S., & Bartels, J. 1940, Geomagnetism (Oxford: Clarendon Press)
Cillié, G. 1932, MNRAS, 92, 820
Ding, M. D., & Fang, C. 1996, A&A, 314, 643
Ding, M. D., Fang, C., & Yun, H. S. 1999, ApJ, 512, 454
Donati-Falchi, A., Falciani, R., & Smaldone, L. A. 1984, A&A, 131, 256
Emslie, A. G., & Machado, M. E. 1979, Sol. Phys., 64, 129
Fang, C., & Ding, M. D. 1995, A&AS, 110, 99
Fletcher, L., & Hudson, H. 2001, Sol. Phys., 204, 69
Greene, J. M. 1988, J. Geophys. Res., 93, 8583
Gregory, S. E., Myers, D., Tarbell, T., McIntosh, S., & Bush, R. 2001, AGU Fall Meeting, abstract SH42A-0765
Handy, B. N. 1998, Ph.D. thesis, Montana State Univ.
Handy, B. N., et al. 1999, Sol. Phys., 187, 229
Hudson, H. S. 1972, Sol. Phys., 24, 414
Hudson, H. S., Acton, L. W., Hirayama, T., & Uchida, Y. 1992, PASJ, 44, L77
Kaufmann, P., et al. 2002, ApJ, 574, 1059
Kosugi, T., et al. 1991, Sol. Phys., 136, 17
Lau, Y.-T., & Finn, J. M. 1991, ApJ, 366, 577
Lin, R. P., & Hudson, H. S. 1976, Sol. Phys., 50, 153
Machado, M. E., & Hénoux, J.-C. 1982, A&A, 108, 61
Machado, M. E., & Rust, D. M. 1974, Sol. Phys., 38, 499
Machado, M. E., et al. 1986, in The Lower Atmosphere of Solar Flares, ed. D. F. Neidig (Sunspot: NSO), 483
Matthews, S. A., van Driel-Gesztelyi, L., Hudson, H. S., & Nitta, N. V. 2002, in Multi-Wavelength Observations of Coronal Structure and Dynamics, ed. P. C. H. Martens & D. P. Cauffman (Amsterdam: Pergamon), 289
Metcalf, T. R., Canfield, R. C., Avrett, E. H., & Metcalf, F. T. 1990a, ApJ, 350, 463
Metcalf, T. R., Canfield, R. C., & Saba, J. L. R. 1990b, ApJ, 365, 391
Metcalf, T. R., Hudson, H. S., Kosugi, T., Puetter, R. C., & Piña, R. K. 1996, ApJ, 466, 585
Neidig, D. F., & Kane, S. R. 1993, Sol. Phys., 143, 201
Neidig, D. F., & Wiborg, P. H., Jr. 1984, Sol. Phys., 92, 217
Osterbrock, D. E. 1989, Astrophysics of Gaseous Nebulae and Active Galactic Nuclei (Mill Valley: University Science Books)
Rust, D. M., & Hegwer, F. 1975, Sol. Phys., 40, 141
Sylwester, B., & Sylwester, J. 2000, Sol. Phys., 194, 305
Tandberg-Hanssen, E., & Emslie, A. G. 1988, The Physics of Solar Flares (Cambridge: Cambridge Univ. Press)